Computers and Fluids 124 (2016) 226–236

Contents lists available at ScienceDirect

Computers and Fluids

journal homepage: www.elsevier.com/locate/compfluid

Lattice Boltzmann simulation of particle-laden turbulent channel flow

Lian-Ping Wang [a,b,*], Cheng Peng [a], Zhaoli Guo [b], Zhaosheng Yu [c]

[a] Department of Mechanical Engineering, 126 Spencer Laboratory, University of Delaware, Newark, Delaware 19716–3140, USA
[b] National Laboratory of Coal Combustion, Huazhong University of Science and Technology, Wuhan, P.R. China
[c] Department of Mechanics, Zhejiang University, 310027 Hangzhou, China

ARTICLE INFO

Article history:
Received 24 December 2014
Revised 13 May 2015
Accepted 6 July 2015
Available online 21 July 2015

Keywords:
Particle-laden flow
Turbulent channel flow
Lattice Boltzmann equation
Finite-size effect
Particle–particle interactions
Particle-resolved simulation

ABSTRACT

Modulation of the carrier phase turbulence by finite-size solid particles is relevant to many industrial and environmental applications. Here we report particle-resolved simulations of a turbulent channel flow laden with finite-size solid particles. We discuss how the mesoscopic lattice Boltzmann method (LBM) can be applied to treat both the turbulent carrier flow and moving fluid-particle interfaces. To validate the LBM approach, we first simulate the single-phase turbulent channel flow at a frictional Reynolds number of 180. A non-uniform force field is designed to excite turbulent fluctuations. The resulting mean flow profiles and turbulence statistics were found to be in excellent agreement with the published data based on the Chebychev-spectral method. We also found that the statistics of the fully-developed turbulent channel flow are independent of the setting of some of the relaxation parameters in the LBM approach. We then consider a particle-laden turbulent channel flow under the same body force. The particles have the same density as the fluid. The particle diameter is 5% of the channel width and the average volume fraction is 7.09%. We found that the presence of the particles reduces the mean flow speed by 4.6%, implying that the fluid-particle system is more dissipative than the single-phase flow. The maximum local reduction of the mean flow speed is about 7.5%. The effects of the solid particles on the fluid rms velocity fluctuations are mixed: both reduction and augmentation are observed depending on the direction and spatial location relative to the channel walls. Overall, particles enhance the relative turbulence intensity in the near wall region and suppress the turbulence intensity in the center region. The particle concentration distribution across the channel is also complicated. We find that there is a dynamic equilibrium location resembling the Segŕe–Silberberg effect known for a laminar wall-bounded flows. Our LBM results were found to be in good agreement with results based on a finite-difference method with direct forcing to handle the moving solid particles. Additionally, phase-partitioned statistics are obtained and compared.

1. Introduction

Turbulent flows laden with solid particles or liquid droplets are ubiquitous in engineering, biological and environmental applications. A turbulent particle-laden flow system is more complicated than its single-phase counterpart owing to a wider range of length and time scales and the additional parameters associated with the dispersed phase [1]. For a turbulent flow laden with non-deforming spherical particles, the length scales range from the particle diameter (d_p) and flow Kolmogorov length (η) to the integral length scale (L). When d_p/η is small and the volume fraction (ϕ) of the dispersed phase is low, the response of a particle to the local flow can be well described by an equation of motion [3], making it unnecessary to resolve the disturbance flow on the scale of the particle size. Most theoretical understanding for turbulent particle-laden flows has been developed based on these assumptions. Computationally, the condition of $d_p/\eta < 1$ partially justifies the use of point-particle based simulation (PPS) [2]. In the last 25 years, PPS has enabled researchers to discover and quantify a number of important phenomena in turbulent particle-laden flows including preferential concentration [4,5], turbulence modulation by inertial particles [6,7], particle deposition rate, and turbulent collision rate of inertial particles [2,8–11].

In many applications, the particle size is comparable to or larger than the flow Kolmogorov length [12], which introduces a finite-size effect greatly complicating the description of the flow system. Currently, the only rigorous method is to numerically resolve the disturbance flows around particles, known as the particle-resolved simulation (PRS). This requires an explicit implementation of the no-slip boundary condition on the surface of each moving particle.

* Corresponding author at: Department of Mechanical Engineering, 126 Spencer Laboratory, University of Delaware, Newark, Delaware 19716-3140, United States. Tel.: +3028318160.
E-mail addresses: lwang@udel.edu (L.-P. Wang), cpengxpp@udel.edu (C. Peng), zlguo@hust.edu.cn (Z. Guo), yuzhaosheng@zju.edu.cn (Z. Yu).

http://dx.doi.org/10.1016/j.compfluid.2015.07.008
0045-7930/

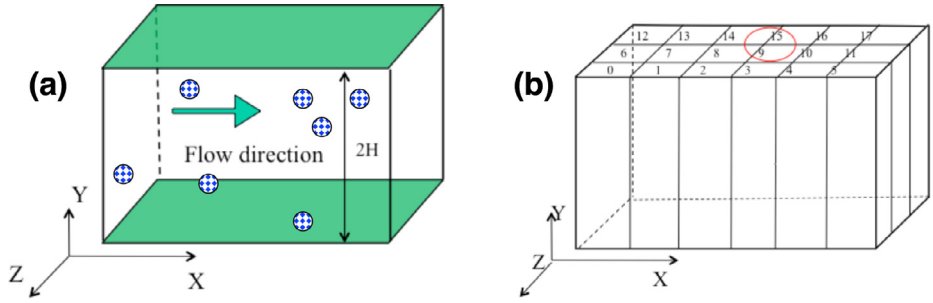

Fig. 1. Sketches of (a) the coordinate system used for the channel flow simulation and (b) the 2D domain decomposition for MPI parallel implementation.

PRS of turbulent particle-laden flows requires direct simulation of the turbulent carrier flow and explicit and accurate treatment of many moving fluid-solid interfaces, such that all scales from the turbulence integral scale to the dissipation scales and particle size are adequately resolved with realistic scale separations that depend on applications. In recent years, several PRS methods based on the Navier–Stokes (N–S) equation have been developed, with the particle-fluid interfaces treated by the immersed boundary method [13,14], direct-forcing [15], local analytical treatment [16], overset grid [12], force-coupling [17], or penalization method [18]. As reviewed in [19,20], these studies have contributed to the understanding of flow modulation by the inertial particles and the dynamic effects due to finite particle size.

As an alternative approach, the lattice Boltzmann method (LBM) has also been applied as a PRS method for turbulent particle-laden flows [19–22]. The LBM approach features a high-level data locality essential to efficient implementation of PRS. Another advantage is that LBM has the flexibility and simplicity (i.e., via local bounce-back) for implementing interfacial boundary conditions. This offers the potential for the method to be applied to treat turbulent flows laden with non-spherical and deformable particles.

The main objective of this paper is to explore the use of LBM for simulating wall-bounded turbulent particle-laden flows. Previously, we have applied LBM to homogeneous isotropic particle-laden turbulent flows [19,20]. In a wall-bounded flow, the flow scale near the wall and away from the wall could be quite different, and to authors' knowledge, there has not been a successful simulation of a particle-laden turbulent channel flow using LBM. There are, however, particle-resolved simulations of such flows based on pseudo-spectral and finite-difference methods with the moving particles treated by the immersed boundary method [14,23,24] or direct forcing method [15].

From an experimental perspective, particle-laden wall-bounded flows have played an important role in understanding turbulence modulation by solid particles. Previous experimental studies included particle-laden open channel flow [25], turbulent boundary layer [26,27], and turbulent pipe flow [28,29]. It is well known that the presence of small solid particles typically decreases the turbulence intensity due to enhanced viscous dissipation, whereas large particles can enhance the turbulence intensity due to undamped disturbances and wake effects [30,31]. Solid particles have also been observed to alter the critical Reynolds number for laminar to turbulent flow transition, where small particles delay transition to larger flow Reynolds numbers, and large particles cause transition at smaller Reynolds numbers [32]. In general, the nature and level of modulation depend on many factors including scales and geometric configurations of the carrier phase flow, particle characteristics such as size, density, mass loading, particle distribution, and gravity. Finite-size particles may introduce both local viscous dissipation and kinetic energy production. Experimental studies mainly provide bulk flow statistics, however, they could not reveal detailed interactions between particles and turbulence at the scale of particle size. It is hoped that particle-resolved direct numerical simulations can provide a deep understanding of turbulence modulation by solid particles and effects of finite particle size on the dynamics of solid particles.

The paper is organized as follows. In Section 2, the physical problem and the LBM model are described, along with important implementation details that lead to successful simulations of the particle-laden turbulent channel flow. The results are presented in Section 3, where we first discuss results from simulations of single-phase turbulent channel flow, by comparing our results with benchmark data. We then analyze in some detail one simulation of particle-laden turbulent channel flow at $d_p/(2H) = 0.05$, where H is channel half width. A summary and main conclusions are presented in Section 4.

2. Problem statement and the simulation method

We consider a turbulent channel flow laden with finite-size particles, as sketched in Fig. 1(a), with x, y, and z representing the streamwise, transverse, and spanwise directions, respectively. The width of the channel is $2H$, and the domain size in the streamwise direction is L_x and in the spanwise is L_z. The turbulent flow is driven by a constant body force (or equivalently mean pressure gradient) in the x direction. Periodic boundary condition is assumed in the x and z directions, and the no-slip condition on the two channel walls.

For the single-phase turbulent channel flow (*i.e.*, without solid particles), the flow is mainly governed by the flow Reynolds number $Re = \overline{U}H/\nu$, where ν is the kinematic viscosity and $\overline{U}$ is the mean flow speed. At the fully developed stage, force balance $2\tau_w L_x L_z = \rho g 2 H L_x L_z$ leads to the expressions for the wall viscous shear stress τ_w and frictional velocity u^* as

$$\tau_w = \rho g H, \quad u^* = \sqrt{\frac{\tau_w}{\rho}} = \sqrt{Hg}, \tag{1}$$

where ρ is the fluid density and g is the body force per unit mass. The frictional Reynolds number is $Re_\tau = u^* H/\nu = H/(\nu/u^*)$, where ν/u^* is the length unit in the viscous sublayer. The large-scale eddy-turnover time is defined as H/u^*.

In this paper, we only consider neutrally buoyant solid particles of identical diameter d_p and density $\rho_p = \rho$. To keep the flow driving force for the particle-fluid system the same, the same body force g is applied in the x direction inside the solid particles. The only difference from the single-phase flow is then the presence of the moving fluid-solid interfaces where the no-slip condition is to be satisfied. There are two new governing parameters in the particle-laden flow. The first is the particle size relative to the half channel width d_p/H. The second is the volume fraction of the particulate phase, $\phi_V = n\pi d_p^3/6$, where n is the particle number density.

2.1. The lattice Boltzmann method (LBM)

In this paper, we wish to develop a numerical method to solve the turbulent particle-laden channel flow stated above, with local flow

around each particle resolved. Following our recent studies [19,20], the multiple-relaxation-time (MRT) lattice Boltzmann method [33] is applied for this particle-resolved turbulent flow simulation. Since a thorough discussion of the method including a few validation cases have already been presented in [19,20], here we only summarize the essential components of the method.

The MRT LBM solves the evolution of mesoscopic particle distribution function by a lattice Boltzmann equation

$$\mathbf{f}(\mathbf{x}+\mathbf{e}_\alpha\delta t, t+\delta t) = \mathbf{f}(\mathbf{x},t) - \mathbf{M}^{-1}\cdot\mathbf{S}\cdot[\mathbf{m}-\mathbf{m}^{(\mathrm{eq})}] + \mathbf{Q}. \tag{2}$$

where $\mathbf{e}_\alpha$ are microscopic velocities, δt is the lattice time step, $\mathbf{M}$ is an orthogonal transformation matrix converting the distribution function $\mathbf{f}$ from discrete velocity space to moment space $\mathbf{m}$, in which the collision relaxation is performed. The term $\mathbf{Q}$ denotes a forcing field in the mesoscopic phase space to produce a desired non-uniform, time-dependent, large-scale physical space forcing field $\rho_0\mathbf{q}(\mathbf{x},t)$. Its implementation follows the MRT formulation [34,35] that is free of low-order discrete lattice errors, and the implementation details including the exact form and efficient computational implementation were discussed in Section 2.2 of [20].

The basic idea of MRT is that the streaming sub-step is handled in the microscopic lattice-velocity space but the collision sub-step is performed in the moment space. The transformation between the microscopic velocity space and the moment space is carried out by matrix operations as $\mathbf{m}=\mathbf{M}\cdot\mathbf{f}$, $\mathbf{f}=\mathbf{M}^{-1}\cdot\mathbf{m}$. The diagonal relaxation matrix $\mathbf{S}$ specifies the relaxation rates for the non-conserved moments.

The macroscopic hydrodynamic variables, including density ρ, momentum, and pressure p, are obtained from the moments of the mesoscopic distribution function $\mathbf{f}$. In the nearly incompressible formulation [36], they are given as

$$\rho = \rho_0 + \delta\rho, \quad \rho_0 = 1; \quad \delta\rho = \sum_\alpha f_\alpha,$$
$$\rho_0\mathbf{u} = \sum_\alpha f_\alpha\mathbf{e}_\alpha + \frac{\delta t}{2}\rho_0\mathbf{q}(\mathbf{x},t), \quad p = \delta\rho c_s^2 \tag{3}$$

where $\mathbf{u}$ is the macroscopic fluid velocity, and the sound speed c_s is equal to $1/\sqrt{3}$ in lattice units. In our implementation, the distribution functions $\mathbf{f}$ are solved only at the fluid lattice nodes.

We shall state all design details of the model. The D3Q19 model was used and $\mathbf{e}_\alpha$ represents the discrete lattice velocities, given as

$$\mathbf{e}_\alpha = \begin{cases} (0,0,0), & \alpha = 0 \\ (\pm1,0,0),\ (0,\pm1,0),\ (0,0,\pm1) & \alpha = 1,2,\ldots,6, \\ (\pm1,\pm1,0),\ (\pm1,0,\pm1),\ (0,\pm1,\pm1) & \alpha = 7,8,\ldots,18. \end{cases} \tag{4}$$

The 19 orthogonal moments

$$\mathbf{m} = (\widetilde{\rho}, e, \varepsilon, j_x, q_x, j_y, q_y, j_z, q_z, 3p_{xx}, 3\pi_{xx}, p_{ww}, \pi_{ww}, p_{xy}, p_{yz}, p_{xz}, m_x, m_y, m_z)^T \tag{5}$$

are defined through the element of the transformation matrix (each subscript runs from 0 to 18) as

$$M_{0,\alpha} = ||\mathbf{e}_\alpha||^0, \quad M_{1,\alpha} = 19||\mathbf{e}_\alpha||^2 - 30,$$
$$M_{2,\alpha} = \big(21||\mathbf{e}_\alpha||^4 - 53||\mathbf{e}_\alpha||^2 + 24\big)/2$$
$$M_{3,\alpha} = e_{\alpha x}, \quad M_{5,\alpha} = e_{\alpha y}, \quad M_{7,\alpha} = e_{\alpha z},$$
$$M_{4,\alpha} = \big(5||\mathbf{e}_\alpha||^2 - 9\big)e_{\alpha x}, \quad M_{6,\alpha} = \big(5||\mathbf{e}_\alpha||^2 - 9\big)e_{\alpha y},$$
$$M_{8,\alpha} = \big(5||\mathbf{e}_\alpha||^2 - 9\big)e_{\alpha z}, \tag{6}$$

$$M_{9,\alpha} = 3e_{\alpha x}^2 - ||\mathbf{e}_\alpha||^2, \quad M_{11,\alpha} = e_{\alpha y}^2 - e_{\alpha z}^2, \tag{7}$$

$$M_{13,\alpha} = e_{\alpha x}e_{\alpha y}, \quad M_{14,\alpha} = e_{\alpha y}e_{\alpha z}, \quad M_{15,\alpha} = e_{\alpha x}e_{\alpha z}, \tag{8}$$

$$M_{10,\alpha} = \big(3||\mathbf{e}_\alpha||^2 - 5\big)\big(3e_{\alpha x}^2 - ||\mathbf{e}_\alpha||^2\big),$$
$$M_{12,\alpha} = \big(3||\mathbf{e}_\alpha||^2 - 5\big)\big(e_{\alpha y}^2 - e_{\alpha z}^2\big), \tag{9}$$

$$M_{16,\alpha} = \big(e_{\alpha y}^2 - e_{\alpha z}^2\big)e_{\alpha x}, \quad M_{17,\alpha} = \big(e_{\alpha z}^2 - e_{\alpha x}^2\big)e_{\alpha y},$$
$$M_{18,\alpha} = \big(e_{\alpha x}^2 - e_{\alpha y}^2\big)e_{\alpha z}. \tag{10}$$

The equilibrium moments are defined as

$$\widetilde{\rho}^{(eq)} = \widetilde{\rho} = \delta\rho, \quad e^{(eq)} = -11\delta\rho + \frac{19}{\rho_0}\big(j_x^2 + j_y^2 + j_z^2\big),$$
$$\varepsilon^{(eq)} = \omega_\varepsilon\delta\rho + \frac{\omega_{\varepsilon j}}{\rho_0}\big(j_x^2 + j_y^2 + j_z^2\big),$$
$$j_x^{(eq)} = j_x = \rho_0 u_x, \quad j_y^{(eq)} = j_y = \rho_0 u_y, \quad j_z^{(eq)} = j_z = \rho_0 u_z,$$
$$q_x^{(eq)} = -\frac{2}{3}j_x, \quad q_y^{(eq)} = -\frac{2}{3}j_y, \quad q_z^{(eq)} = -\frac{2}{3}j_z, \tag{11}$$

$$p_{xx}^{(eq)} = \frac{1}{3\rho_0}\big[2j_x^2 - \big(j_y^2 + j_z^2\big)\big], \quad p_{ww}^{(eq)} = \frac{1}{\rho_0}\big[j_y^2 - j_z^2\big], \tag{12}$$

$$p_{xy}^{(eq)} = \frac{1}{\rho_0}j_x j_y, \quad p_{yz}^{(eq)} = \frac{1}{\rho_0}j_y j_z, \quad p_{xz}^{(eq)} = \frac{1}{\rho_0}j_x j_z, \tag{13}$$

$$\pi_{xx}^{(eq)} = \omega_{xx}p_{xx}^{(eq)}, \quad \pi_{ww}^{(eq)} = \omega_{xx}p_{ww}^{(eq)}, \tag{14}$$

$$m_x^{(eq)} = m_y^{(eq)} = m_z^{(eq)} = 0, \tag{15}$$

with the following relaxation parameters

$$\mathbf{S} = \mathrm{diag}(0, s_1, s_2, 0, s_4, 0, s_4, 0, s_4, s_9, s_{10}, s_9, s_{10}, s_{13}, s_{13}, s_{13}, s_{16}, s_{16}, s_{16}). \tag{16}$$

The kinematic viscosity ν of the model is given as $\nu = \big(s_9^{-1} - 1\big)c_s^2\delta t$.

It is noted that some of the relaxation parameters do not affect the simulated flow, but may affect the numerical stability of the code. To examine if the results change with different settings, we will test three versions of the model in the simulation of single-phase turbulent channel flow, as given by the specific model parameters in Table 1. They will be labeled as MRT, BGK, and MRT-LD (low dissipation). The parameters for the case label as MRT are taken from [33] and those marked as MRT-LD are from [37]. The special case of BGK assumes all relaxation parameters are equal to s_9. The setting labeled as MRT intends to optimize the numerical stability based on the linear analysis, while the MRT-LD setting minimizes the numerical dissipation by using a smaller bulk viscosity. For simulations of turbulent

Table 1
Parameter settings and simulated statistics.

Label	ω_ε	$\omega_{\varepsilon j}$	ω_{xx}	s_1	s_2	s_4	s_9	s_{10}	s_{13}	s_{16}
MRT [33]	0.0	$-\frac{475}{63}$	0.0	1.19	1.4	1.2	$\frac{\delta t}{3\nu+0.5\delta t}$	1.4	s_9	1.6
BGK	3.0	$-\frac{11}{2}$	$-\frac{1}{2}$	s_9	s_9	s_9	$\frac{\delta t}{3\nu+0.5\delta t}$	s_9	s_9	s_9
MRT-LD [37]	3.0	$-\frac{11}{2}$	$-\frac{1}{2}$	1.8	s_1	s_9	$\frac{\delta t}{3\nu+0.5\delta t}$	s_1	s_9	s_1

flow or turbulent particle-laden flow, we found that MRT is numerically much more stable than BGK, although their levels of accuracy are similar. In term of computational time, the overhead for MRT is typically about 20% when compared to the BGK collision model. The above completes the description of the D3Q19 MRT LBM model.

When moving particles are present, additional implementation details need to be considered. The no-slip condition at the moving fluid-particle interfaces are treated by a quadratic interpolated bounce-back scheme [38]. When a particle moves, a solid lattice node may become a fluid node with unknown distribution functions. The missing distribution functions for the new fluid lattice node are constructed by a new velocity-constrained extrapolation method to be discussed below (Section 2.2). The hydrodynamic force $\mathbf{F}_i$ and torque $\mathbf{\Gamma}_i$ acting on the ith particle are calculated during the interpolated bounce-back procedure by the recently-developed Galilean invariant momentum exchange method [39,40]. It is very important that we enforce the local Galilean invariance property in order to produce physically correct results, as discussed in Peng et al. [40]. The particle translational velocity, position, angular velocity and displacement are then updated as,

$$\begin{aligned}\mathbf{V}_i^{t+\delta t} &= \mathbf{V}_i^t + \frac{1}{M_p}\left(\frac{\mathbf{F}_i^{t+\delta t/2}+\mathbf{F}_i^{t-\delta t/2}}{2}+\sum_j \mathbf{F}_{ij}^t\right)\delta t,\\ \mathbf{Y}_i^{t+\delta t} &= \mathbf{Y}_i^t + \frac{1}{2}\left(\mathbf{V}_i^t+\mathbf{V}_i^{t+\delta t}\right)\delta t,\end{aligned} \tag{17}$$

$$\begin{aligned}\mathbf{\Omega}_i^{t+\delta t} &= \mathbf{\Omega}_i^t + \frac{1}{I_p}\left(\frac{\mathbf{\Gamma}_i^{t+\delta 2/2}+\mathbf{\Gamma}_i^{t-\delta t/2}}{2}\right)\delta t,\\ \mathbf{\Theta}_i^{t+\delta t} &= \mathbf{\Theta}_i^t + \frac{1}{2}\left(\mathbf{\Omega}_i^t+\mathbf{\Omega}_i^{t+\delta t}\right)\delta t,\end{aligned} \tag{18}$$

where M_p and $I_p \equiv \frac{2}{5}M_p R_i^2$ are the mass and moment of inertia of the i^{th} particle, R_i is the particle radius, and $\mathbf{F}_{ij}$ represents unresolved interaction force acting on the ith particle due to its interaction with jth particle (e.g., the lubrication force correction, see [41,42]). In this study, a simple pair-wise repulsive force model, the same as what was used in [19], was applied to prevent particles from overlapping.

2.2. The velocity-constrained normal extrapolation refilling

This refilling scheme is based on the normal extrapolation refilling scheme proposed in [38]. First, the link direction $\mathbf{e}_c$ that maximizes the quantity $\vec{n}\cdot\mathbf{e}_c$ is identified, where $\vec{n}$ denotes the outward unit normal to the local solid surface from where the new fluid point was uncovered. After determining the direction $\mathbf{e}_c$, all unknown distribution functions at the new fluid node (marked by a square in Fig. 2) are obtained by a quadratic extrapolation using three nodes (marked by the circles in Fig. 2)

$$\begin{aligned}\hat{f}_\alpha(\mathbf{x}_{new}, t+\delta t) = {} & 3f_\alpha(\mathbf{x}_{new}+\mathbf{e}_c\delta t, t+\delta t)\\ & -3f_\alpha(\mathbf{x}_{new}+2\mathbf{e}_c\delta t, t+\delta t)\\ & +f_\alpha(\mathbf{x}_{new}+3\mathbf{e}_c\delta t, t+\delta t).\end{aligned} \tag{19}$$

When two particles are close and the information at a fluid lattice node is not available, the order of the interpolation is reduced to the linear interpolation or the simple bounce-back. It is recognized that the distribution functions after this first step may not precisely satisfy the Dirichlet boundary condition at the new fluid node, which is very close to the wall node marked by a blue triangle. In MRT LBM, we can take advantage of the fact that the velocity can be constrained to the wall velocity without changing other macroscopic properties (such as pressure and stress components). Therefore, in the second step, we first computed all moments at the new fluid node by multiplying the transfer matrix $\mathbf{M}$ as

$$\mathbf{m}(\mathbf{x}_{new}, t+\delta t) = \mathbf{M}\hat{\mathbf{f}}(\mathbf{x}_{new}, t+\delta t) \tag{20}$$

where $\hat{\mathbf{f}}$ indicates the temporary distribution function after the unconstrained normal extrapolation. Next, we enforced the no-slip boundary condition by constraining the momentum moments

$$j_x = \rho_0 u_{x,w}, \quad j_y = \rho_0 u_{y,w}, \quad j_z = \rho_0 u_{z,w}. \tag{21}$$

Under the nearly incompressible formulation, this is equivalent to constraining the velocity to the local velocity $(u_{x,w}, u_{y,w}, u_{z,w})$ at the wall node. Finally, transfer the moments $\mathbf{m}^*$ after the above modification back to the distribution functions as

$$\mathbf{f}(\mathbf{x}_{new}, t+\delta t) = \mathbf{M}^{-1}\mathbf{m}^*(\mathbf{x}_{new}, t+\delta t) \tag{22}$$

where $\mathbf{m}^*$ means the moment vector after the velocity is constrained. In this procedure, except the velocity, no other macroscopic quantities are changed.

We find that this constraint significantly reduces the fluctuations in the hydrodynamic forces compared to the unconstrained normal extrapolation. Even more importantly, before introducing this constrained scheme, we used equilibrium plus non-equilibrium refilling [43] and encountered numerical instability that causes the code to diverge. After replaced by the velocity-constrained normal extrapolation refilling, our particle-laden turbulent channel flow code has a much better numerical stability.

The MRT LBM code was parallelized using 2D domain decomposition where the domain is divided in x and z directions as shown in Fig. 1(b). Since the data communications are with the neighboring subdomains only, a nearly ideal scalability could be realized using 1D, 2D and 3D domain decompositions, see discussions in Section 2.3 of Wang et al. [20]. The 2D domain decomposition was chosen here because of the use of an MPI interface code for FFT (Fast Fourier Transform) in data post-processing subroutines, for which the 2D domain decomposition was found to be optimal [44].

2.3. Method to excite transition to turbulence

We have simulated both single-phase and particle-laden turbulent channel flows, as the single-phase flow provides a reference flow to study turbulence modulation by finite-size solid particles. We initialize the flow field using a prescribed mean flow as

$$U^+(y^+) = \begin{cases} y^+ & \text{if } y^+ \le 10.8,\\ \dfrac{1}{0.41}\ln(y^+) + 5.0 & \text{if } y^+ > 10.8,\end{cases} \tag{23}$$

where all quantities with a superscript $+$ are normalized by the wall length unit ν/u^* or velocity unit u^*. While in the particle-laden flow, the disturbances due to the solid particles provide a natural mechanism to excite the flow instability that will lead to a turbulent flow. In the single-phase flow simulation, we must design a mechanism to inject perturbations to the flow to excite flow instability.

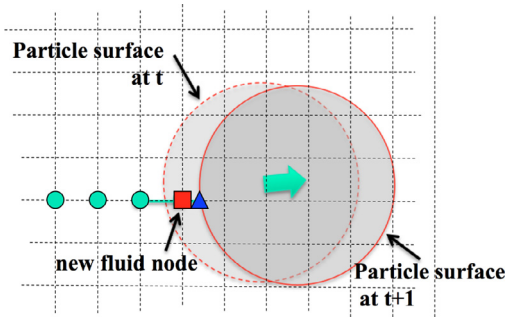

Fig. 2. Sketch to illustrate the refilling scheme.

Table 2
Parameter settings and simulated statistics.

Run	$N_x \times N_y \times N_z$	ν	$u*$	Re_τ	$\delta y/(\nu/u^*)$ (< 2.25 [47])	d_p/H	ϕ_V
Single-phase MRT	$400 \times 199 \times 200$	0.0036	0.006513	180	1.806	–	–
Single-phase BGK	$400 \times 200 \times 200$	0.0036	0.00648	180	1.806	–	–
Single-phase MRT-LD	$400 \times 200 \times 200$	0.0036	0.00648	180	1.806	–	–
MRT-PL	$600 \times 299 \times 300$	0.0040	0.004816	180	1.204	0.1003	7.09%

We add a non-uniform, divergence-free forcing field to the flow for some period of time. Namely, for $h_0 < y < h + h_0 < H$,

$$q_x = g\left[1 - A_0\frac{L_x}{\beta}\sin\left(\frac{2\pi(y-h_0)}{h}\right)\sin\left(\beta\frac{2\pi x}{L_x}\right)\cos\left(\gamma\frac{2\pi z}{L_z}\right)\right] \tag{24}$$

$$q_y = g\frac{A_0}{2}h\left[1 - \cos\left(\frac{2\pi(y-h_0)}{h}\right)\right]\cos\left(\beta\frac{2\pi x}{L_x}\right)\cos\left(\gamma\frac{2\pi z}{L_z}\right) \tag{25}$$

$$q_z = g\frac{A_0}{2}\frac{L_z}{\gamma}\sin\left(\frac{2\pi(y-h_0)}{h}\right)\cos\left(\beta\frac{2\pi x}{L_x}\right)\sin\left(\gamma\frac{2\pi z}{L_z}\right) \tag{26}$$

and for $2H - h_0 - h < y < 2H - h_0$,

$$q_x = g\left[1 + A_0\frac{L_x}{\beta}\sin\left(\frac{2\pi(2H-y-h_0)}{h}\right) \times \sin\left(2\pi\beta\left(\frac{x}{L_x}+\psi\right)\right)\cos\left(\gamma\frac{2\pi z}{L_z}\right)\right] \tag{27}$$

$$q_y = g\frac{A_0}{2}h\left[1 - \cos\left(\frac{2\pi(2H-y-h_0)}{h}\right)\right] \times \cos\left(2\pi\beta\left(\frac{x}{L_x}+\psi\right)\right)\cos\left(\gamma\frac{2\pi z}{L_z}\right) \tag{28}$$

$$q_z = g\frac{A_0}{2}\frac{L_z}{\gamma}\sin\left(\frac{2\pi(2H-y-h_0)}{h}\right) \times \cos\left(2\pi\beta\left(\frac{x}{L_x}+\psi\right)\right)\sin\left(\gamma\frac{2\pi z}{L_z}\right) \tag{29}$$

where $A_0 = \left(\beta\widetilde{A}_0/L_x\right)\sin(2\pi t/T)$ with T being a prescribed period, ψ is a random number between 0 and 1 to introduce a random phase shift, and $\widetilde{A}_0, T, \beta, \gamma, h, h_0$ are prescribed constants. Typically, we set, in lattice units, $h_0 = 2$, $h = H/4$, $\widetilde{A}_0 = 40$, $T = 2000$, $\beta = 3$, and $\gamma = 2$. The magnitude of forcing as reflected by $\widetilde{A}_0$ is quite large. The parameters used here were chosen by trial-and-error to ensure a rapid development of turbulence without causing numerical instability. When the nonlinear flow instability is excited, we switch off the non-uniform forcing by setting $A_0 = 0$ and the flow is only driven by the constant body force g.

3. Results

In this section, we present results on both single-phase and particle-laden turbulent channel flows. We are interested in flow statistics when the flow becomes stationary, namely, the driving force is balanced by the net viscous dissipation in the flow. In this preliminary study, we discuss results from four simulations as shown in Table 2: three simulations for single-phase turbulent channel flow corresponding to the model parameters described in Table 1, and one for particle-laden turbulent channel flow. The frictional Reynolds number is set to 180. The fluid viscosity is set above the limiting value 0.00254 [33] when the MRT model may become unstable. Note that the grid resolution is quantified by the value of $\delta y u^*/\nu$, where δy is the grid spacing. Based on the simulations using the BGK LBM model, Lammers et al. [47] suggested that this value should be less than 2.25.

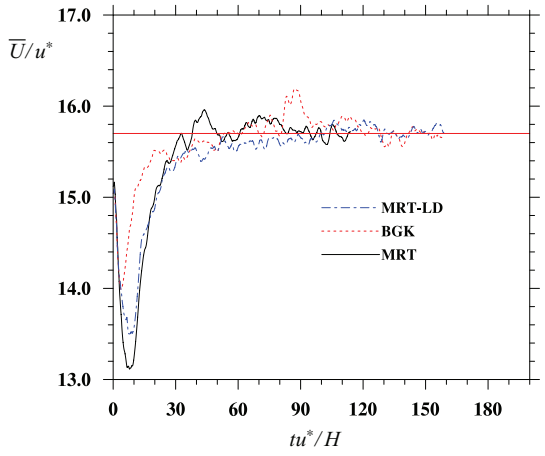

Fig. 3. Time evolution of the mean flow velocity for the simulated single-phase turbulent channel flow. The thin red line marked the long-time average of $\langle U\rangle/u^* = 15.7$. (For interpretation of the references to colour in this figure legend, the reader is referred to the web version of this article).

3.1. Single-phase turbulent channel flow

In the three single-phase flow simulations shown in Table 2, the physical settings are essentially the same, the only difference is in the specification of model parameters (Table 1). Initially, we used a grid resolution $400 \times 200 \times 200$ for a computational domain with $L_x = 4H$ and $L_z = 2H$. The viscosity was set to 0.0036 and the body force g was determined by $g = \left(\nu H^{-1.5} Re_\tau\right)^2$. During the simulation, we monitor the maximum local Mach number ($|\mathbf{u}|_{\max}/c_s$) and the maximum density fluctuations $\delta\rho_{\max}$ to make sure that they remain small.

Interestingly, we found that the single-phase MRT run became numerically unstable and the run diverged after about 5,000 time steps. Visualizations of the flow velocity field show a chequerboard instability [45,46] with a clear chequerboard pattern oriented at $\pm 45^o$, while the other two runs are stable. The cause for the chequerboard instability could be that an even lattice number in the wall-normal direction led to the reflected acoustic wave to be in phase with the original acoustic oscillations. This problem was somewhat unexpected, but was fixed by simply changing the domain size in y to 199. This is the reason for the minor differen ce in grid resolutions shown in Table 2.

Applying the Reynolds decomposition and noting that the flow is homogeneous in x and z directions, we can write $u_x = U(y) + u_x'(x,y,z)$, $u_y = u_y'(x,y,z)$, $u_z = u_z'(x,y,z)$, $p = P(y) + p'(x,y,z)$, where $U(y)$ and $P(y)$ are the mean flow velocity and pressure, respectively. In Fig. 3, we show the mean flow speed (averaged over y) as a function of non-dimensional time $t^* \equiv tu^*/H$. The

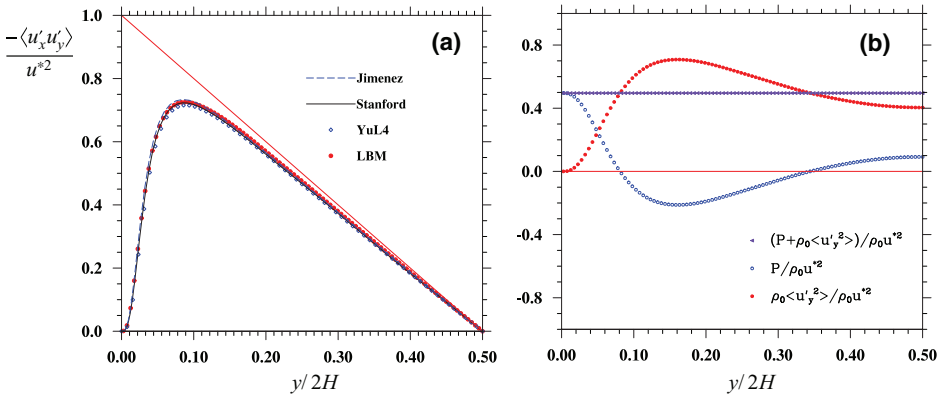

Fig. 4. (a) Turbulent Reynolds stress profile in half the channel, (b) Mean pressure distribution and transverse mean-square fluctuation velocity profiles in half the channel. All quantities are normalized by u^{*2}. The data are averaged over $110 < t^* < 150$. The thin red line in (a) denotes the total shear stress, so the difference between this straight line and the data represents the viscous shear stress due to the mean flow. (For interpretation of the references to colour in this figure legend, the reader is referred to the web version of this article).

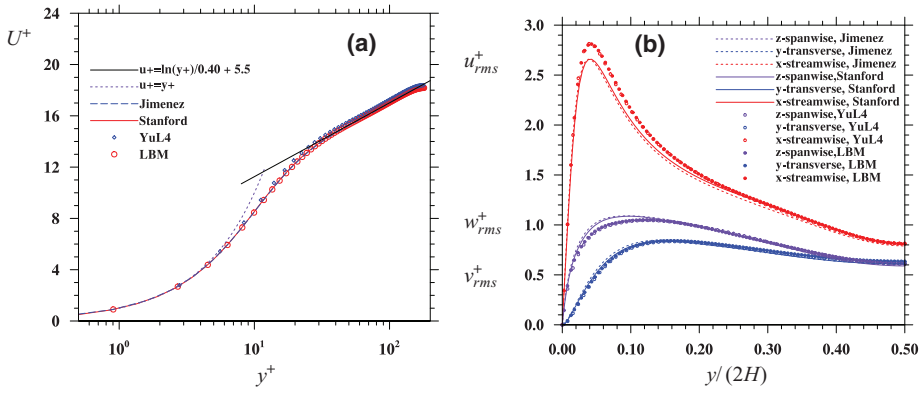

Fig. 5. (a) The mean flow velocity profiles, (b) r.m.s. velocity profiles from the single-phase MRT run. The data are averaged over $110 < t^* < 150$. The results from the single-phase BGK run and the single-phase MRT-LD run are essentially identical.

nonuniform force field to excite the turbulent flow is only applied for $0 < t^* < 3.24$. During this period of extra forcing, the mean flow speed decreases and kinetic energy is quickly transferred from the mean flow to the turbulent fluctuations. After $t^* = 3.24$, for the MRT and MRT-LD runs, there is a further reduction in the mean flow speed (possibly due to shifting of intense vertical structures towards the channel walls immediately after the nonuniform force field is switched off) before the mean flow rebounds and gradually reaches a stationary value of about $15.7u^*$. It is evident that the flow reaches a statistically stationary stage at around $t^* = 50$. All three runs converge to the same average mean speed. Although not explicitly shown here, we compare various profiles from the three runs and found that they are essentially identical. For this point on, only results from the MRT run will be reported.

For this channel flow, we can show that the x-momentum balance equation becomes

$$0 = \frac{d\langle -u_x' u_y' \rangle}{dy} + g + \nu \frac{d^2 U}{dy^2}, \tag{30}$$

which leads to the total stress (Reynolds plus viscous) distribution as

$$\frac{1}{u^{*2}}\left[\langle -u_x' u_y' \rangle + \nu \frac{dU}{dy}\right] = -\frac{y_c}{H}, \tag{31}$$

where y_c is the distance relative to the channel center, and y is the distance from a wall. Fig. 4(a) compares our simulated Reynolds stress profile in half of the channel with several benchmark results at the same Re_τ. The channel center is at $y/(2H) = 0.5$. Throughout the paper, "Stanford" refers to the data from the Chebychev-spectral simulation done by the Stanford group [48,49] using a domain size $4\pi H \times 2H \times 4\pi H/3$, "Jimenez" denotes the data from the Chebychev-spectral simulation done by Jimenez et al. [50,51] using a domain size $4\pi H \times 2H \times 4\pi H/3$, "YuL4" indicates data from a second-order finite-difference simulation by Yu et al. [15] using a domain size $4H \times 2H \times 2H$ (identical to ours). Although our domain size is smaller than the domain size in the Chebychev-spectral simulations, the results are in excellent agreement with the Chebychev-spectral simulation results. This could demonstrate that the MRT LBM scheme has less numerical diffusion than the finite-difference method which shows a slightly smaller maximum Reynolds stress.

The y-momentum balance equation is

$$\frac{\partial}{\partial y}\left[\langle u_y'^2 \rangle + \frac{P}{\rho_0}\right] = 0, \tag{32}$$

which shows that $P(y) + \rho_0\langle u_y'^2 \rangle = \text{constant}$. Fig. 4(b) shows the profiles of $P(y)$ and $\rho_0\langle u_y'^2 \rangle$ over half of the channel, as well as the sum. Several observations can be made. First the sum is indeed a constant and equal to 0.4913. Second, the transverse velocity fluctuation reaches a maximum at around $y/(2H) = 0.14$, corresponding to a minimum mean pressure. Third, the mean normalized pressure integrated over y was found to be around 10^{-6}, which is essentially zero. This is expected as the total mass is conserved by the mid-link bounce-back.

Next, we show the mean velocity profile on a log-linear plot in Fig. 5(a). In wall units, the channel center is at $y^+ = 180$. Once again, our LBM result is in excellent agreement with the spectral simulation results. The profile fits well the standard linear viscous sublayer scaling for $y^+ < 5$, and the inertial sublayer scaling starting at $y^+ > 30$.

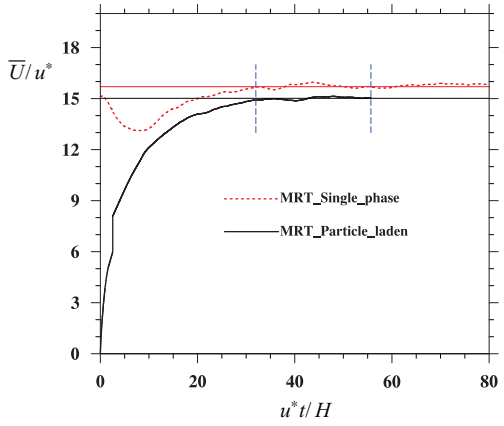

Fig. 6. The time evolution of mean flow speed (averaged over y) in the turbulent particle-laden flow. The two blue dash lines indicate the stationary stage ($32.2 < t^* < 56.1$). The two horizontal lines mark 15.74 and 15.02, respectively. (For interpretation of the references to colour in this figure legend, the reader is referred to the web version of this article).

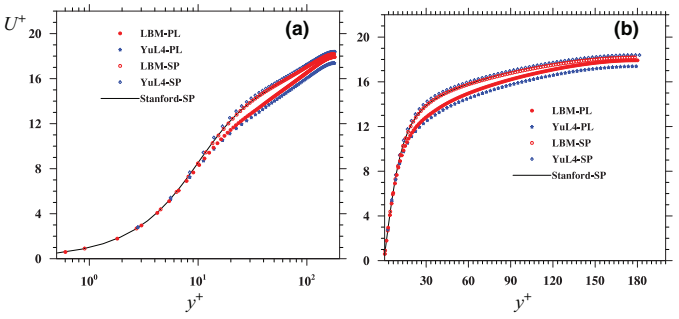

Fig. 7. The mean velocity profile for the particle-laden flow run: (a) log-linear plot; (b) linear-linear plot. The data are averaged over $32.2 < t^* < 56.1$. Also shown are other profiles for comparison including the results from the finite-difference method [15].

Yu et al.'s finite-difference result appears to slightly over-predict the mean velocity for $y^+ > 5$. The average flow speeds in our LBM, Yu et al., Standford, and Jimenez are 15.65, 15.84, 15.69, and 15.60, respectively. Note that the two Chebychev-spectral simulations use a non-uniform grid, so a cubic spine interpolation is first used to obtain the velocity at the same uniform y^+ locations as in Yu et al.'s before the average flow speed is processed.

The root-mean-squared velocity profiles are shown in Fig. 5(b). Here $u^+_{rms} \equiv \sqrt{\langle u_x'^2\rangle}/u^*$, $v^+_{rms} \equiv \sqrt{\langle u_y'^2\rangle}/u^*$, and $w^+_{rms} \equiv \sqrt{\langle u_z'^2\rangle}/u^*$. Overall, the profiles from different studies are in reasonable agreement. Our LBM results are in excellent agreement with the results of Yu et al., for all three components. Since both our simulation and Yu et al.'s are based on a smaller domain size, the difference between our results and the Chebychev-spectral results are likely due to the use of different computational domain sizes. Our LBM data show a slightly larger streamwise rms velocity and slightly smaller spanwise rms velocity.

In summary, our LBM simulations for single-phase turbulent channel flow are validated by comparing with data from published spectral and finite-difference simulations.

3.2. Particle-laden turbulent channel flow

Next we present preliminary results for the particle-laden turbulent channel flow. The physical parameters were shown on the last row in Table 2. Note that the resolution is increased by 50% in each direction when compared to the single phase flow simulation to better resolve the disturbance flows due to solid particles and to overcome potential numerical stability. We will compare directly our LBM results to those of the finite-difference results [15] where the moving particles are treated by a direct forcing method.

3.2.1. Turbulence modulation

In Fig. 6, we plot the average mean flow speed as a function of time. For the particle-laden flow simulation, the initial flow velocity is zero, the same body force (could be made larger than g during the developing stage to accelerate the transition and development) is applied to generate the flow. Suspended particles provide the natural mechanism to excite the turbulent fluctuations. The phase-average flow speed (averaged over the fluid lattice points only), $\overline{U}/u^*$, for the particle-laden flow is 15.02, which is 4.6% smaller than the value (15.74) for the single-phase turbulent channel flow. All results presented are based on a time average in the interval $31.9 < t^* < 53.9$.

The fluid-phase-averaged mean flow profile and rms fluctuation velocities are shown in Fig. 7. Also shown for comparison are data from the finite-difference method, for both the single-phase and particle-laden flows. While in the linear viscous sublayer, the velocity profile is unchanged by the presence of the solid particles, in the inertial sublayer, the mean flow speed is reduced. The strongest modulation to the mean flow occurs in the region ($10 < y^+ < 100$) between the wall and the channel centerline.

To better quantify the modulation of the mean flow velocity by the presence of solid particles, we compare changes in flow speed relative to the single-phase flow in Fig. 8. Due to the change of resolution (Table 2), the y^+ positions for the single-phase flow simulation could be different from the locations where the particle-laden flow data are computed. A linear interpolation is used to interpolate the particle-laden flow data to match the same locations used for the single-phase flow. Also added to the plots are results from Yu et al. based on a larger domain size ($8H \times 2H \times 4H$), denoted by YuL8. The relative changes are always computed based on results of the single-phase and particle-laden flows using a same domain size. The computed relative changes of the local mean flow speed from our

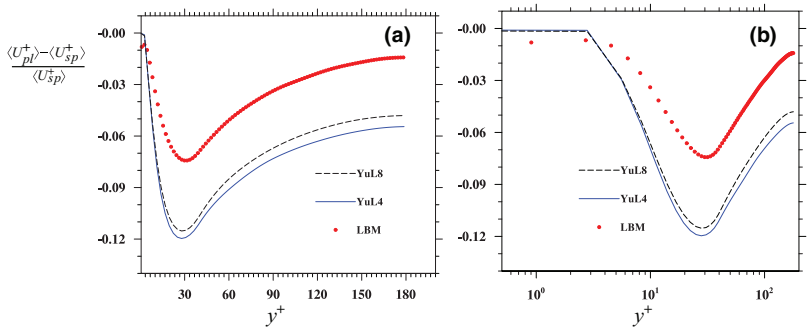

Fig. 8. The relative change in the mean velocity of the flow due to the presence of particles: (a) linear–linear plot; (b) log-linear plot. The data are averaged over $32.2 < t^* < 56.1$.

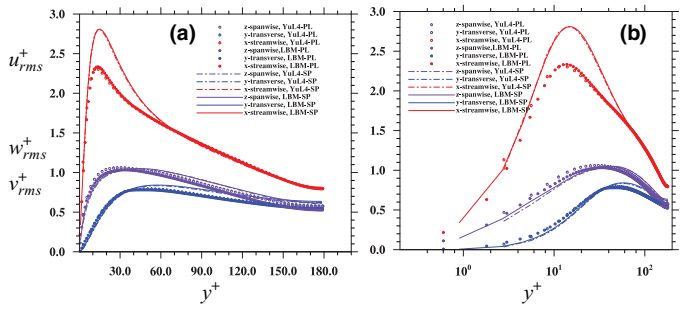

Fig. 9. The r.m.s. velocity profiles in the particle-laden flow: (a) linear–linear plot; (b) log-linear plot. Other results are also plotted for comparison. The data are averaged over $32.2 < t^* < 56.1$.

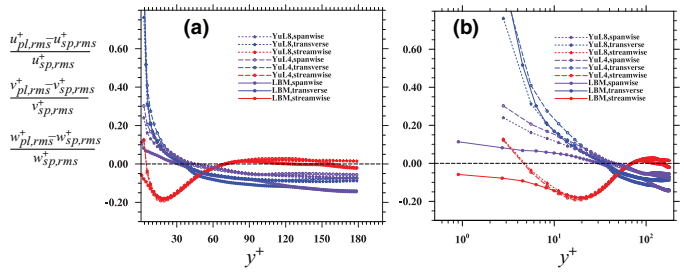

Fig. 10. The relative changes of r.m.s. velocity fluctuations due to the presence of solid particles, relative to the single-phase flow: (a) linear–linear plot; (b) log-linear plot. The data are averaged over $32.2 < t^* < 56.1$.

LBM simulation are qualitatively similar to Yu et al.'s data. Quantitatively, our results show significant less reduction in the mean flow velocity at almost all locations. The maximum changes in the mean flow speed is about 7.5% in our simulation (or 11.96% (L4) to 11.53% (L8) in Yu et al.'s simulations), which occurs at $y^+ \approx 30$. The location of the maximum corresponds to the maximum local particle concentration (see Fig. 11 later). Therefore, the particle–particle hydrodynamic interactions may alter the local mean flow speed. This difference between ours and Yu et al.'s is originated from a larger mean flow velocity for the single-phase flow and a smaller mean velocity in the particle-laden case in the finite-difference approach. The reason for this difference is not clear. The results from Yu et al. for two domain sizes (YuL4 and YuL8) show that the effect of domain size on the relative reduction is not significant in their simulations.

The rms velocity profiles are shown in Fig. 9 on both linear–linear and log-linear plots. The data from both single-phase and particle-laden flows are shown from our LBM and Yu et al.'s finite-difference simulations using the same domain size. In general, all the rms profiles are in excellent agreement. In the streamwise direction, the presence of particles reduces the rms velocity significantly for $y^+ < 70$, with almost no effect near the channel center. However, in the spanwise direction, the rms velocity is augmented by the particles in the near wall region ($y^+ < 30$). This is more clearly seen in Fig. 10 where the percentages of change relative to the single-phase flow are shown. In the outer region, the spanwise velocity fluctuation is slightly reduced. The effect of particles on the transverse rms velocity is somewhat similar to the effect on the spanwise rms velocity, with the augmentation taking place in an even wider region (up to $y^+ \approx 40$). The relative changes in rms velocities from our simulations and the finite-difference simulations are in good quantitative agreement, confirming that the nature of turbulence modulation depends on both location relative to the wall and the spatial direction. Again the effect of computational domain size on the relative changes (particle-laden vs single-phase) is not significant when the results from Yu et al. based on two domain sizes are compared. The main differences between our results and Yu et al.'s occur in the near wall

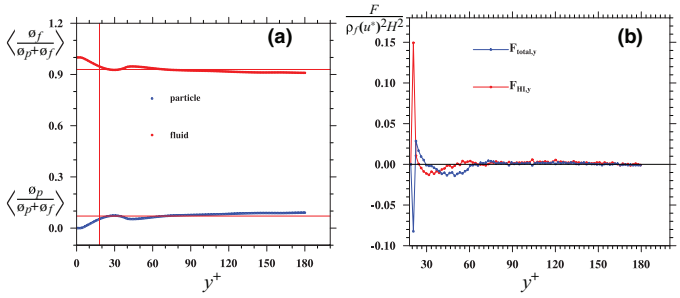

Fig. 11. (a) The local volume fractions of the particulate phase and the fluid phase. (b) The average forces acting on the particle along transverse direction. The data are averaged over $32.2 < t^* < 56.1$ in (a) and over $41.6 < t^* < 56.1$ in (b).

regions (Fig. 10b). Very close to the wall, the finite-difference results show an augmentation of the rms velocity even in the streamwise direction, which is not the case in our LBM simulation. The finite-difference results also show a larger augmentation of rms velocity in the spanwise direction near the wall.

3.2.2. Particle distribution

An interesting question is whether the particles are distributed uniformly or clustered near the wall (which is typically found in point-particle simulations). Fig. 11(a) shows the fraction of space taken up by particle and by fluid nodes, as a function of y^+. Due to the finite size, the particle fraction ϕ_p is zero at $y^+ = 0$. The vertical thin line marks the location of $y = 0.5d_p$. The particle fraction increases near the wall and reach a maximum that is 103.10% of the mean value, at $y/d_p = 0.82$ or $y^+ = 29.50$. It then decreases and reaches a minimum that is 74.47% of the mean value, at $y/d_p = 1.22$ or $y^+ = 43.95$. There is a very gradual increase in ϕ_p when y^+ is increased from 44 to 120. In the center region ($y^+ > 120$), the particle fraction is nearly uniform and is 123.41% of the mean.

The results indicate that there is a quasi-equilibrium position at $y/d_p = 0.82$ or $y^+ = 29.50$, similar to the Segré–Silberberg effect known for laminar wall-bounded flows [52,53]. This is confirmed by the hydrodynamic force and total force (plus the lubrication force) in the transverse direction in Fig. 11(b), as a function of the center position of the solid particles. Here the center positions of the solid particles are divided into bins of width $\Delta y^+ \approx 3.5$, and the average force are computed by averaging over all particles with the centers sitting in a given bin. Here a positive force is a force directed into the wall and negative away from the wall. The lubrication force includes the repulsive forces due to both the particle–particle and particle-wall interactions. The net force crosses zero at $y^+ = 29.50$, corresponding roughly to the location of maximum ϕ_p. There is a region ($29.5 < y^+ < 65$) where the net force is negative, and in this region particles on average move towards to the center region of the channel. In the center region, $y^+ > 120$, the net force is essentially zero, indicating that particles on average are uniformly distributed.

3.2.3. Phase-partitioned statistics

We shall now partition the flow domain into the fluid nodes and nodes covered by the solid particles. The velocity inside a solid particle is given by translation plus solid body rotation, and vorticity inside is defined as twice the angular velocity. Statistics averaged within the lattice points inside the solid particles are to be compared with the fluid-phase averaged statistics discussed in Section 3.2.1. Fig. 12(a) shows the mean velocity profiles averaged over the fluid nodes and over the solid nodes. Very close to the wall, the particle mean flow speed is significantly larger than the fluid velocity, implying that there is a slip between the particle motion and the wall. In the intermediate region ($19.87 < y^+ < 46.35$), the fluid velocity exceeds the particle velocity. Then in the center region, they reach to

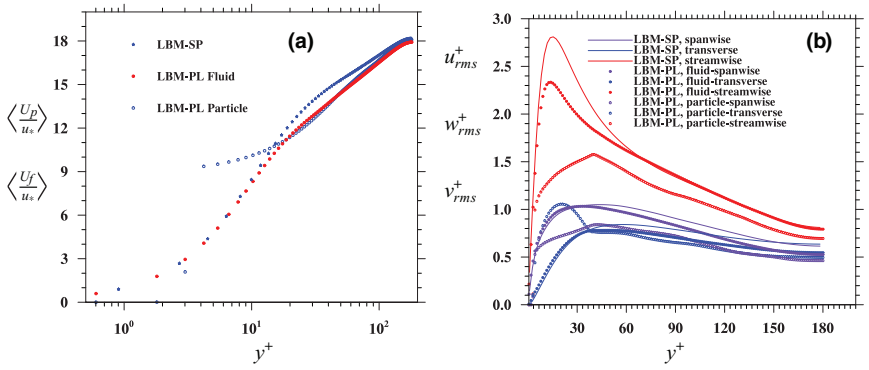

Fig. 12. (a) The phase-partitioned mean velocity profiles. (b) The phase-partitoned r.m.s velocity profiles. The data are averaged over $41.6 < t^* < 56.1$.

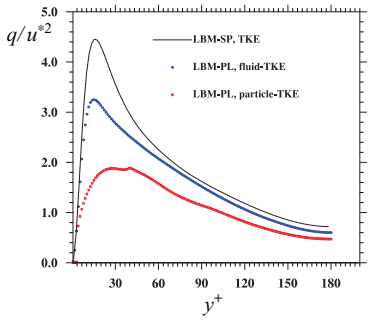

Fig. 13. The phase-partitioned turbulent kinetic energy profiles. The data are averaged over $41.6 < t^* < 56.1$. The result of the single-phase flow is also shown for comparison.

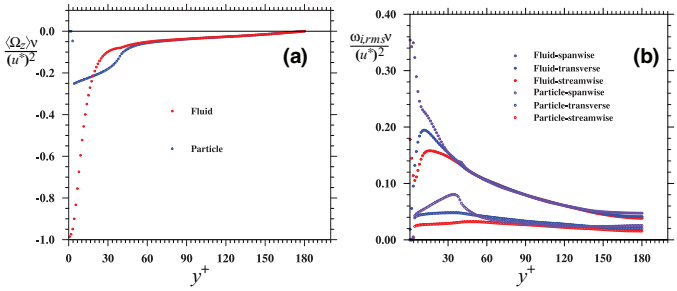

Fig. 14. (a) The phase-partitioned mean vorticity profiles. (b) The phase-partitioned r.m.s vorticity profiles. The mean vorticity is anti-symmetric with respect to the centerline, only the bottom half of the channel is shown. The data are averaged over $41.6 < t^* < 56.1$.

a mutual equilibrium, with particle velocity slightly larger than the fluid velocity (about 0.9%).

The comparison of the rms velocity fluctuations between the two phases is provided by Fig. 12(b). In both the streamwise and spanwise directions, there is a significant difference between the fluid velocity fluctuation and the particle velocity fluctuation, due to the finite-size effect. There is no difference in inertia between the solid particle and the fluid, but the fluid inertia due to the relative motion between the fluid and the particle also contributes to the reduction of particle rms velocity. Clearly, solid particles follow the mean motion of the fluid much more closely than the fluid velocity fluctuations. The most interesting one is the comparison in the transverse direction. The particle rms velocity is significantly larger than the fluid rms velocity for $y^+ < 36.72$, but they are similar outside this region. This interesting larger transverse particle velocity fluctuation near the wall could be related to the sweeping and ejection associated with large-scale flow dynamics in the near-wall region. Clearly, the particulate phase can bring more kinetic energy into the wall region by both the augmented particle mean flow velocity and particle transverse velocity fluctuation. The presence of particles also makes the flow velocity fluctuations more isotropic. The profiles for the particulate phase show a bump at $y+ = 40.33$, close to the location where the local particle volume fraction is peaked.

The phase-partitioned net kinetic energy $q = (\langle u_x'^2 \rangle + \langle u_x'^2 \rangle + \langle u_z'^2 \rangle)/2$ for each phase is compared in Fig. 13, along with the result from the single-phase flow. The fluid-phase kinetic energy is not altered very close to the wall, but it reduced significantly in most parts of the channel. The presence of solid particles contributes to this reduction. Since the mean flow is reduced (Fig. 8), this implies that the relative turbulence intensity is slightly increased near the wall.

The mean vorticity profiles are contrasted in Fig. 14(a). The top two curves represent profiles for the top half channel, and the bottom two for the lower half channel. y^+ is always measured from the wall in each case. The profiles are antisymmetric with respect to the center of the channel. In terms of the magnitude, the two phases have identical mean (and linear) vorticity distribution for $y^+ > 60$. Interestingly, for the intermediate region ($18.7 < y^+ < 47.6$, the upper bound is based on the mean particle vorticity being 20% larger than that of the fluid vorticity), the particle mean vorticity exceeds that of the fluid, indicating that some fast-rotating particles from the near-wall region are being transported into this intermediate region. Finally, in the region very close to the wall ($y^+ < 18.7$), the mean vorticity of the fluid is significantly larger as finite-size particles only respond to the *local-volume-averaged* fluid vorticity. Near the wall, particle rotation is inhibited by the wall.

Finally, the rms vorticity profiles are compared in Fig. 14(b). The particle rms vorticity is roughly half of the corresponding fluid rms vorticity, clearly due to the finite-size (finite-volume) filtering and other effects such as the fluid inertia effect. Unlike the rms velocity, the rms vorticity is nearly isotropic for the region $y^+ > 30$ for the fluid phase (and $y^+ > 60$ for the particulate phase). Near the wall, the spanwise rms vorticity is the largest, followed by the transverse rms vorticity. The streamwise rms vorticity is the smallest. The fluid rms vorticities in the streamwise and spanwise directions exhibit a peak in the near wall region. There is also the peak in the particle rms vorticity in the spanwise direction, but the peak location is further away from the wall at $y^+ = 34.3$.

4. Summary and outlook

The research was motivated by the desire to simulate wall-bounded turbulent particle-laden flows with the fluid-moving solid interfaces directly resolved. We have developed a multiple-relaxation-time lattice Boltzmann approach for this purpose. An important implementation issue is to accurately resolve the moving interfaces, which has been discussed in detail in a separate paper [40]. Specifically, we wish to note that a Galilean invariant momentum exchange method [39] has been implemented, and a

velocity-constrained normal extrapolation refilling is developed to fill populations at the new fluid nodes. These details not only allow the method to produce correct results, but also make the simulations numerically more stable.

To validate the LBM approach, we first simulated the single-phase turbulent channel flow at $Re_\tau = 180$. A non-uniform force field was designed to excite turbulent fluctuations. Three different versions of the collision treatment (i.e., the optimized MRT [33], MRT with low dissipation [37], and BGK) were tested. While not shown in the paper, we found that the statistics of the fully-developed turbulent channel flow are independent of the setting of some of the relaxation parameters. Interestingly, we encountered a checkerboard instability with the optimized MRT setting, and this problem was solved by using an odd number of grid points in the transverse direction. The resulting mean flow profiles and turbulence statistics were found to be in excellent agreement with the published data based on the Chebychev-spectral method, although the domain size we used in this preliminary study was relatively small.

We then considered a particle-laden turbulent channel flow under the same body force used to drive the single-phase flow. The particles have a same density as the fluid. The particle diameter is 5% of the channel width and average volume fraction at 7.09%. We found that the presence of the particles reduce the mean flow speed by 4.6%, implying that the fluid-particle system is more dissipative than the single-phase flow. The maximum local reduction of the mean flow speed is about 7.5%. The effects of the solid particles on the fluid rms velocity fluctuations are mixed: both reduction and augmentation are observed depending on the direction and spatial location relative to the channel walls. Overall, particles enhance the relative turbulence intensity in the near wall region and suppress turbulence in the center region. Particles then play a role of bringing more kinetic energy into the near wall region. This general observation is consistent with experimental observations in wall-bounded particle-laden flows [28]. The particle concentration distribution across the channel is also complicated. We found that there is a dynamic equilibrium location resembling the Segfe–Silberberg effect known for a laminar wall-bounded flows [52,53]. Our LBM results were compared to separate results using a finite-difference method with direct forcing to handle the moving solid particles [15]. While the results on the reduction of mean flow velocity are quantitatively different, the results on the modulation of flow rms velocities from the two numerical approaches are in good quantitative agreement. The relative changes due to the presence of particles are not sensitive to the computational domain size, partially justifying the use of a smaller domain size in this study.

We also examined the phase-partitioned statistics and found that there is a finite slip between the particle mean motion and the channel wall. The particle transverse rms velocity is significantly larger than the fluid transverse rms velocity. The presence of solid particles tends to help mix the flow in the wall region with the flow in the center region, and also make the flow more isotropic. The mean vorticities for the two phases are the same for the center region. In the intermediate region ($18.7 < y^+ < 47.6$), the particle mean vorticity can exceed the fluid mean vorticity. The particle rms vorticity is much less than the fluid rms vorticity due to finite-size filtering.

From the above results, it is clear that LBM has the potential to accurately and efficiently treat particle-laden turbulent flows. This study represents our first effort in applying LBM to wall-bounded turbulent particle-laden flows. Only one mesh resolution was considered for the particle-laden flow case. Based on our prior experience [20], the local profiles very close to a solid particle surface may require a higher resolution. Nevertheless, the average field statistics of the kind reported in this paper do not depend much on the grid resolution. It is also desirable to consider local mesh refinement around a moving solid particle [54]. We are in the process of optimizing our simulation code so we can carry out a variety of simulations covering different flow and particle parameter regimes. Some additional results regarding the effect of particle size can be found in [55]. We are also exploring a possibility to use a cuboid mesh so that the mesh size in the wall normal direction is different from these in the other two periodic directions.

Acknowledgements

This work has been supported by the U.S. National Science Foundation (NSF) under grants CBET-1235974 and AGS-1139743 and by Air Force Office of Scientific Research under grant FA9550-13-1-0213. LPW also acknowledges support from the Ministry of Education of P.R. China and Huazhong University of Science and Technology through Chang Jiang Scholar Visiting Professorship. Computing resources are provided by National Center for Atmospheric Research through CISL-P35751014, and CISL-UDEL0001 and by University of Delaware through NSF CRI 0958512.

References

[1] Balachandar S, Eaton JK. Turbulent dispersed multiphase flow. Annu Rev Fluid Mech 2010;42:111–33.
[2] Wang L-P, Rosa B, Gao H, He GW, Jin GD. Turbulent collision of inertial particles: point-particle based, hybrid simulations and beyond. Int J Multiphase Flow 2009;35:854–67.
[3] Maxey MR, Riley JJ. Equation of motion for a small rigid sphere in a nonuniform flow. Phys Fluids 1983;26:883–9.
[4] Squires KD, Eaton JK. Preferential concentration of particles by turbulence. Phys Fluids A 1991;3:1169–79.
[5] Wang L-P, Maxey MR. Settling velocity and concentration distribution of heavy particles in homogeneous isotropic turbulence. J Fluid Mech 1993;256:27–68.
[6] Squires KD, Eaton JK. Particle response and turbulence modification in isotropic turbulence. Phys Fluids A 1990;2:1191–203.
[7] Elghobashi S, Truesdell G. On the two-way interaction between homogeneous turbulence and dispersed solid particles. I: Turbulence modification. Phys Fluids 1993;5:1790–801.
[8] Sundaram S, Collins LR. Collision statistics in an isotropic particle-laden turbulent suspension. Part 1. Direct numerical simulations. J Fluid Mech 1997;335:75–109.
[9] Zhou Y, Wexler AS, Wang L-P. Modelling turbulent collision of bidisperse inertial particles. J Fluid Mech 2001;433:77–104.
[10] Ayala O, Grabowski WW, Wang L-P. A hybrid approach for simulating turbulent collisions of hydrodynamically-interacting particles. J Comput Phys 2007;225:51–73.
[11] Jin GD, He G-W, Wang L-P. Large eddy simulation of collisional statistics of inertial particles in isotropic turbulence. Phys Fluids 2010;22:055106.
[12] Burton TM, Eaton JK. Fully resolved simulations of particle-turbulence interaction. J Fluid Mech 2005;545:67–111.
[13] Uhlmann M. An immersed boundary method with direct forcing for the simulation of particulate flows. J Comp Phys 2005;209:448–76.
[14] Uhlmann M. Interface-resolved direct numerical simulation of vertical particulate channel flow in the turbulent regime. Phys Fluids 2008;20:053305.
[15] Shao X, Wu T, Yu Z. Fully resolved numerical simulation of particle-laden turbulent flow in a horizontal channel at a low Reynolds number. J Fluid Mech 2012;693:319–44. doi:10.1017/jfm.2011.533.
[16] Zhang Z, Prosperetti A. A second-order method for three-dimensional particle simulation. J Comp Phys 2005;210:292–324.
[17] Yeo K, Dong S, Climent E, Maxey MR. Modulation of homogeneous turbulence seeded with finite size bubbles or particles. Int J Multiphase Flow 2010;36:221–33.
[18] Homann H, Bec J. Finite-size effects in the dynamics of neutrally buoyant particles in turbulent flow. J Fluid Mech 2010;651:81–91.
[19] Gao H, Li H, Wang L-P. Lattice boltzmann simulation of turbulent flow laden with finite-size particles. Comp & Math with Applications 2013;65:194–210. doi:10.1016/j.camwa.2011.06.028.
[20] Wang L-P, Ayala O, Gao H, Andersen C, Mathews K. Study of forced turbulence and its modulation by finite-size solid particles using the lattice Boltzmann approach. Comp Math Appl 2014;67:363–80. doi:10.1016/j.camwa.2013.04.001.
[21] Gillissen J. Turbulent drag reduction using fluid spheres. J Fluid Mech 2013;716:83–95.
[22] Ten Cate A, Derksen JJ, Portela LM, van den Akker HEA. Fully resolved simulations of colliding monodisperse spheres in forced isotropic turbulence. J Fluid Mech 2004;519:233–71.
[23] Pan Y, Banerjee S. Numerical investigation of the effects of large particles on wall turbulence. Phys Fluids 1997;9:3786–807.
[24] Vowinckel B, Kempe T, Frhlich J. Fluid-particle interaction in turbulent open channel flow with fully-resolved mobile beds. Adv Water Resources 2014;72:32–44.
[25] Rashidi M, Hetstoni G, Banerjee S. Particle turbulence interaction in a boundary layer. Intl J Multiphase Flow 1990;16:935–49.
[26] Kaftori D, Hetsroni G, Banerjee S. The effect of particles on wall turbulence. Intl J Multiphase Flow 1997;24:359–86.

[27] Rogers CB, Eaton JK. The effect of small particles on fluid turbulence in a flat-plate, turbulent boundary layer in air. Phys Fluids 1991;3:928–37.
[28] Zisselmar R, Molerus O. Investigation of solid-liquid pipe flow with regard to turbulence modification. Chem Engng J 1979;18:233–9.
[29] Belt RJ, Daalmans ACLM, Portela M. Experimental study of particle-driven secondary flow in turbulent pipe flows. J Fluid Mech 2012;709:1–36.
[30] Gore RA, Crowe CT. Effect of particle size on modulating turbulent intensity. Int J Multiphase Flow 1989;15:279–85.
[31] Hetsroni G. Particle turbulence interaction. Intl J Multiphase Flow 1989;15:735–46.
[32] Matas J-P, Morris JF, Guazzelli E. Transition to turbulence in particulate pipe flow. Phys Rev Lett 2003;90:014501.
[33] d'Humières D, Ginzburg I, Krafczyk M, Lallemand P, Luo L-S. Multiple-relaxation-time lattice boltzmann models in three-dimensions. Phil Trans R Soc London A 2002;360:437–51.
[34] Guo Z, Zheng C, Shi B. Discrete lattice effects on the forcing term in the lattice boltzmann method. Phys Rev E 2002;65:046308.
[35] Lu J, Han H, Shi B, Guo Z. Immersed boundary lattice boltzmann model based on multiple relaxation times. Phys Rev E 2012;85:016711.
[36] He X, Luo LS. Lattice boltzmann model for the incompressible navier-stokes equation. J Stat Phys 1997;88:927–44.
[37] Peng Y, Liao W, Luo L-S, Wang L-P. Comparison of the lattice boltzmann and pseudo-spectral methods for decaying turbulence. Part I. Low-order statistics. Comp Fluids 2010;39:568–91.
[38] Lallemand P, Luo L-S. Lattice boltzmann method for moving boundaries. J Comp Phys 2003;184:406–21.
[39] Wen B, Zhang C, Yu Y, et al. Galilean invariant fluid-solid interfacial dynamics in lattice boltzmann simulations. J Comp Phys 2014;266:161–70.
[40] Peng C, Teng Y, Hwang B, Guo Z, Wang L-P. Implementation issues and benchmarking of lattice boltzmann method for moving particle simulations in a viscous flow. Comput Math Appl 2015 submitted.
[41] Nguyen NQ, Ladd AJC. Lubrication corrections for lattice-boltzmann simulations of particle suspensions. Phys Rev E 2002;66:046708.
[42] Dance SL, Maxey MR. Incorporation of lubrication effects into the force-coupling method for particulate two-phase flow. J Comput Phys 2003;189:212–38.
[43] Caiazzo A. Analysis of lattice Boltzmann nodes initialisation in moving boundary problems. Prog Comput Fluid Dyn 2008;8:3–10.
[44] Ayala O, Wang L-P. Parallel implementation and scalability analysis of 3D fast fourier transform using 2D domain decomposition. Parallel Comput 2013;39:58–77.
[45] Kandhai D, Koponen A, Hoekstra A, et al. Implementation aspects of 3D lattice-bgk: Boundaries, accuracy, and a new fast relaxation method. J Comp Phys 1999;150:482–501.
[46] Ohwada T, Asinari P. Artificial compressibility method revisited: Asymptotic numerical method for incompressible Navier-Stokes equations. J Comp Phys 2010;229:1698–723.
[47] Lammers P, Beronov KN, Volkert R, Brenner G, Durst F. Lattice bgk direct numerical simulation of fully developed turbulence in incompressible plane channel flow. Computers Fluids 2006;35:1137–53.
[48] Kim J, Moin P, Moser R. Turbulence statistics in fully-developed channel flow at low reynolds-number. J Fluid Mech 1987;177:133–66.
[49] Moser RD, Kim J, Mansour NN. Direct numerical simulation of turbulent channel flow up to re-tau = 590. Phys Fluids 1999;11:943–5.
[50] Hoyas S, Jimenez J. Reynolds number effects on the Reynolds-stress budgets in turbulent channels. Phys Fluids 2008;20:101511.
[51] Jimenez J, Hoyas S. Turbulent fluctuations above the buffer layer of wall-bounded flows. J Fluid Mech 2008;611:215–36.
[52] Segré G, Silberberg A. Radial particle displacements in poiseuille flow of suspensions. Nature 1961;189:209–10.
[53] Segré G, Silberberg A. Behavior of macroscopic rigid spheres in poiseuille flow. J Fluid Mech 1962;14:136–57.
[54] Chen SY, Peng C, Teng Y, Wang L-P. Improving lattice boltzmann simulation of moving particles in a viscous flow using local grid refinement. Comput Math Appl 2015 Submitted.
[55] Wang L-P, Peng C, Guo ZL, Yu ZS. Flow modulation by finite-size neutrally buoyant particles in a turbulent channel flow. ASME J Fluids Eng 2015 Submitted.